Polarization memory effect in optical coherence tomography and dental imaging application

Yueli Chen
Linda Otis
Quing Zhu

Polarization memory effect in optical coherence tomography and dental imaging application

Yueli Chen,[a,b] **Linda Otis,**[c] **and Quing Zhu**[b]
[a]Agiltron Incorporated, 15 Cabot Road, Woburn, Massachusetts 01801
[b]University of Connecticut, Department of Electrical and Computer Engineering, 371 Fairfield Road, Storrs, Connecticut 06269
[c]University of Maryland, Dental School, 650 West Baltimore Street, Baltimore, Maryland 21201

Abstract. We report the existence of polarization memory effect (PME) in optical coherence tomography and investigate its potential applications in dental imaging. We performed the study in three steps. First, microsphere scattering phantoms of different sizes were imaged in order to validate experimental results with PME theory. Both linearly and circularly polarized light were used to probe the samples. Second, healthy tooth samples were scanned and polarization memory effect was identified in dentin. In this step, specific verification and signal processing were performed to rule out possible image interpretation by birefringence effect. Third, we evaluated dentin demineralization with PME. Results show polarization memory can be useful to characterize this dynamic mineralization process for early caries detection and rehabilitation. © *2011 Society of Photo-Optical Instrumentation Engineers (SPIE).* [DOI: 10.1117/1.3606573]

1 Introduction

Polarization measurement in optical coherence tomography (OCT)[1] offers an additional contrast mechanism. It greatly extends the capability of OCT in biological tissue imaging. In the current literature, birefringence has been frequently used to interpret many polarization-sensitive OCT (PS-OCT) image data. Stokes vector, Jones matrix, and Mueller matrix are used in the mathematical analysis.[2–7] It is a polarization effect that is found in many biological tissues such as skin, nerve fiber, tendon, and muscle.[8–16] When birefringence is strong, the light field vector orientation can be modified periodically within the imaging depth. When birefringence is weak, signal processing such as Stokes and statistical averaging around a small area can still retrieve birefringence contrast for valuable tissue characterization.[17–19] Polarization sensitive detection is also very valuable in dental OCT. Many dental features including dentin, enamel, and their boundaries (dentin-enamel junction), caries lesions, and mineralization progress are more effectively characterized in PS-OCT than that in gray-scale intensity OCT.[20–26]

In this paper, we report on the polarization memory effect (PME) in OCT. Polarization memory was first discovered by MacKintosh et al.[27] in a multiple scattering study of optically dense medium. The study recorded preservation of the polarization state, particularly for circularly polarized light backscattered from turbid samples. This phenomenon was derived through field correlation function rather than imaging data. Ni and Alfano explored the polarization memory effect using a time-resolved system.[28] They compared two phantoms made of scattering particles of different diameters and concluded that

for the larger particle phantom, circularly polarized light had a good "memory" for its helicity and could be used to enhance the image contrast. Compared to the field correlation method, the time-resolved measurement greatly resembles the imaging principle of OCT. To study this memory effect in OCT, we first followed the previous work by probing two microsphere phantoms of different particle sizes using both linearly and circularly polarized light. The back scattered light was collected and analyzed by a coherent PS-OCT detection system. The phantom imaging data was agreeable with the work reported by Ni and Alfano and can be explained by the polarization memory effect. More interestingly, we also found polarization memory in dentin. The imaging feature of PME was visually similar to weak birefringence. When the phase retardation was less than one period (<2 pi) over the axial scan depth, the resulting PS-OCT image produced a similar whitish band-like structure.[17, 18] Therefore, we discussed approaches to differentiate the two polarization effects and showed that the observed polarization feature in dentin was originated from PME. Furthermore, we used PME to study the demineralization process in dentin matrix. The result suggested that the PME could be a new contrast mechanism in the OCT imaging of biological tissues.

2 Theory

Polarization memory describes a phenomenon whereby light retains its incident polarization state after it is backscattered from a turbid medium. It can be explained by the Mie scattering theory under a multiple scattering scenario. In Mie theory, the scattering particle size is a characteristic parameter to determine the fraction of light with an anisotropy factor g that is forward and backward scattered. When the scattering particle size is comparable to the wavelength, g can be close to unity, meaning a

Address all correspondence to: Yueli Chen, University of Connecticut, Research and Development, 371 Fairfield Road, Storrs, Connecticut 06269; Tel: 617-620-6060; Fax: 860-486-2447; E-mail: yueli.mit.chen@gmail.com.
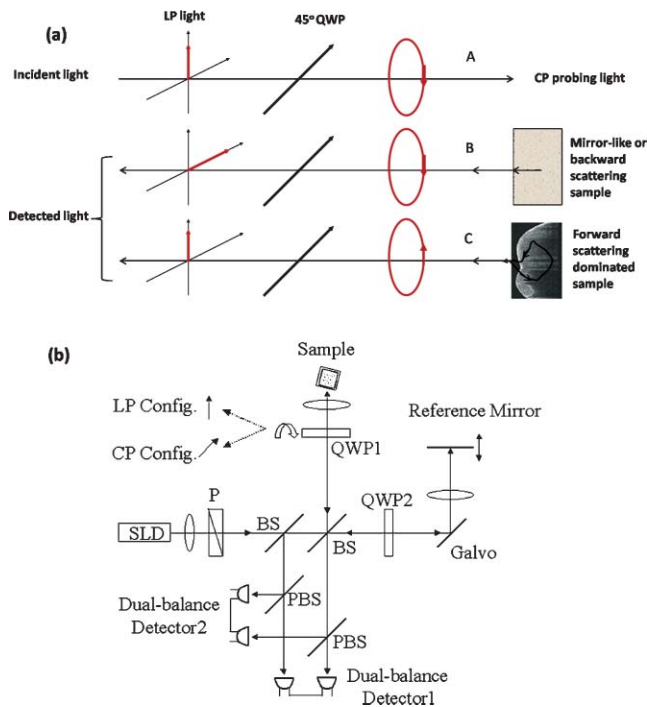
Fig. 1 (a) A diagram shows a simplified picture of polarization memory effect due to multiple forward scattering. (b) Schematic of PS-OCT. Superluminescent diode (SLD); polarizer (P); beam splitter (BS); polarizing beam splitters (PBS); QWP1,QWP2, quarter-wave plates; Galvo, galvanometer. After filtering and A/D conversion, the detected signals are processed by a PC.

major portion of the light is forward scattered. In this condition, polarization memory effect may occur when the randomization of the field propagation direction goes faster than that of the polarization states.[27] This memory effect is particularly interesting when circularly polarized (CP) instead of linearly polarized (LP) light is used, as forward scattering retains the helicity of the incident CP light (defined under a spatially reversed coordinate system) and transfers the light power to the orthogonal polarization channel. Ni and Alfano[28] observed this light power transfer from co-polarized channel to cross-polarized detection channel with CP light, but not LP light. Co-polarized channel herein refers to the channel where the majority of the light power is expected to be detected in a regular backscattering or mirror reflection scenario. Usually, only a small fraction of light would leak to the cross-polarized channel, for example, due to the depolarization process. Figure 1(a) intends to give an overly simplified picture of polarization memory effect. In the incident light path **A**, the vertically polarized light is transferred to the CP probing light with a quarter waveplate oriented at the 45 deg azimuthal angle. In the return path **B**, normal backscattering such as single scattering reverses the helicity of the CP light. After a second pass through the same quarter waveplate, the scattered light is mostly preserved in the horizontal polarization channel. This channel is the co-polarization channel with respect to the initially vertically polarized light. Alternatively, when LP probing light is used by simply removing the quarter waveplate from the optical path, the co-polarization channel will be the vertical channel according to the definition. In the return path **C**, if the light probes a strong forward scattering sample,

it may experience a zigzagged looping path before exiting the sample surface. The returned light will then remember the original helicity and therefore, a significant amount of light power will go to the vertical polarization detection channel after the quarter waveplate. Because of the polarization memory, the light field energy is transferred from the co-polarization channel to the cross-polarization channel. In contrast, LP probing light will not see such a channel energy reversal effect. In this context, a cross-polarization discrimination (XPD) ratio is conveniently defined as:

$$\mathrm{XPD}(z) = 20 \log\left[E_{\mathrm{x-pol}}(z)/E_{\mathrm{co-pol}}(z)\right]. \quad (1)$$

XPD and phase retardation angle[2] have clear physics for PME and birefringence, respectively. From an imaging prospective, the two terms give different mapping functions in PS-OCT. The difference in visualizing two mapping functions in our data is not significant. Therefore, we have used XPD to map PS-OCT images in this paper.

3 Material and Methods

A time-domain PS-OCT system configured with both LP and CP probing light was used to investigate the size-related polarization-sensitive scattering phenomenon [Fig. 1(b)]. A superluminescent diode (SLD) provided the low coherence illumination of 2 mW at 1310 nm. The vertically and horizontally polarized signals were detected simultaneously each with the balanced detection technique. The device had 10 Hz axial scan rate, 3.6 mm scan depth in air, and a sensitivity of 96 dB. Early PS-OCT typically used CP light to probe the sample. In a previous paper,[25] we implemented the LP probing light by simply removing the 45 deg quarter waveplate from the sample arm. In this study, we rotated the fast axis of the waveplate to 0 deg to produce LP probing light. This was to make the experimental parameters such as the optical path delay more identical between the LP and CP configurations.

Two TiO$_2$ microsphere solutions with different particle diameters were purchased from Bangs Lab Inc. as scattering phantoms. One had a particle diameter of 9.9 μm ($g = 0.88$) and the other 0.1 μm particle diameter ($g = 0.018$). The size variances were less than 10%. The microspheres were floating in the deionized water ($n = 1.33$) with 10% volume density. The size difference between the two spheres resulted in very different anisotropy factors g. The samples were held in polarization preserving cuvettes, and during the experiments the cuvettes were slightly tilted to avoid the glass surface reflection.

Tooth imaging was performed using the same PS-OCT system. Five teeth were sectioned in an axial orientation and 37% phosphoric acid gel was placed on the sectioned dentin surface for 60 s and then washed away. This "acid conditioning of a dentin surface" produced micromorphological effects on the dentin surface, removing the organic material within the surface dentinal tubule orifices, as previously shown.[29] In other words, after the gel was placed on the tooth, the surface dentin composed of tubules of mineral hydroxylapatite could lose a significant amount of organic material. Subsequently, OCT scans were taken across the enamel and the mantel dentin. The lesion

region had a slight brownish hue which was helpful in steering the OCT beam through the target.

4 Results and Discussions

Figure 2 shows the depth-resolved backscattering profiles (A-lines) of the microsphere solutions for CP and LP configurations. The rising edges to the left are the front surface of the sphere solution. Figures 2(a) and 2(b) are the A-lines of the two polarization channels obtained from the smaller spheres. The scattered intensity is in units of dB. The polarization remains primarily in the co-polarization channels. Only a small fraction of light power goes to the cross-polarization channels, indicating minor polarization degeneration within the propagation depth. The attenuation profiles of LP and CP light are very similar. They reveal a linear attenuation profile in the logarithm intensity scale that satisfies Beer's law and is consistent with a single scattering model. The attenuation comes from two parts, the absorption of water ($\mu_a \approx 1.2$ cm^{-1}), and the scattering of spheres ($\mu_s \approx 5.38$ cm^{-1}). A linear fit of the experimental curve with system calibration yields a total attenuation coefficient of μ_t 5.93 cm^{-1}, which is roughly the sum of μ_a and μ_s

calculated from Mie theory. The scattering profile of the large sphere is quite different from that of the smaller one, as shown from the XPD curve in Fig. 2(c) and 2(d) where the A-lines of the two channels are placed in the insets. In Fig. 2(d), the XPD curve of LP probing light never exceeds the zero line, but only asymptotically approaches it as the light propagates deeper. This is expected because the cross-polarized channel has a weaker energy than the co-polarized channel. The interesting point here is from the CP measurement as shown in Fig. 2(c): the light energy quickly transfers to the cross-polarized channel and exceeds the energy level of the co-polarized channel. This occurs after a depth of about 100 μm from the liquid-air surface. XPD reaches a peak level of 6 dB above the zero line at a depth of about 200 μm from the liquid-air surface. This channel energy reversal indicates the existence of the polarization memory effect due to forward scattering.[30] PME may be utilized to enhance biomedical imaging. For example, a recent study has shown a significantly improved imaging contrast of a reflective target embedded in liquid.[31]

Dental tissues are known to have strong optical scattering. The hydroxyapatite crystals form the tissue matrix within which active mineralization and demineralization can take place and
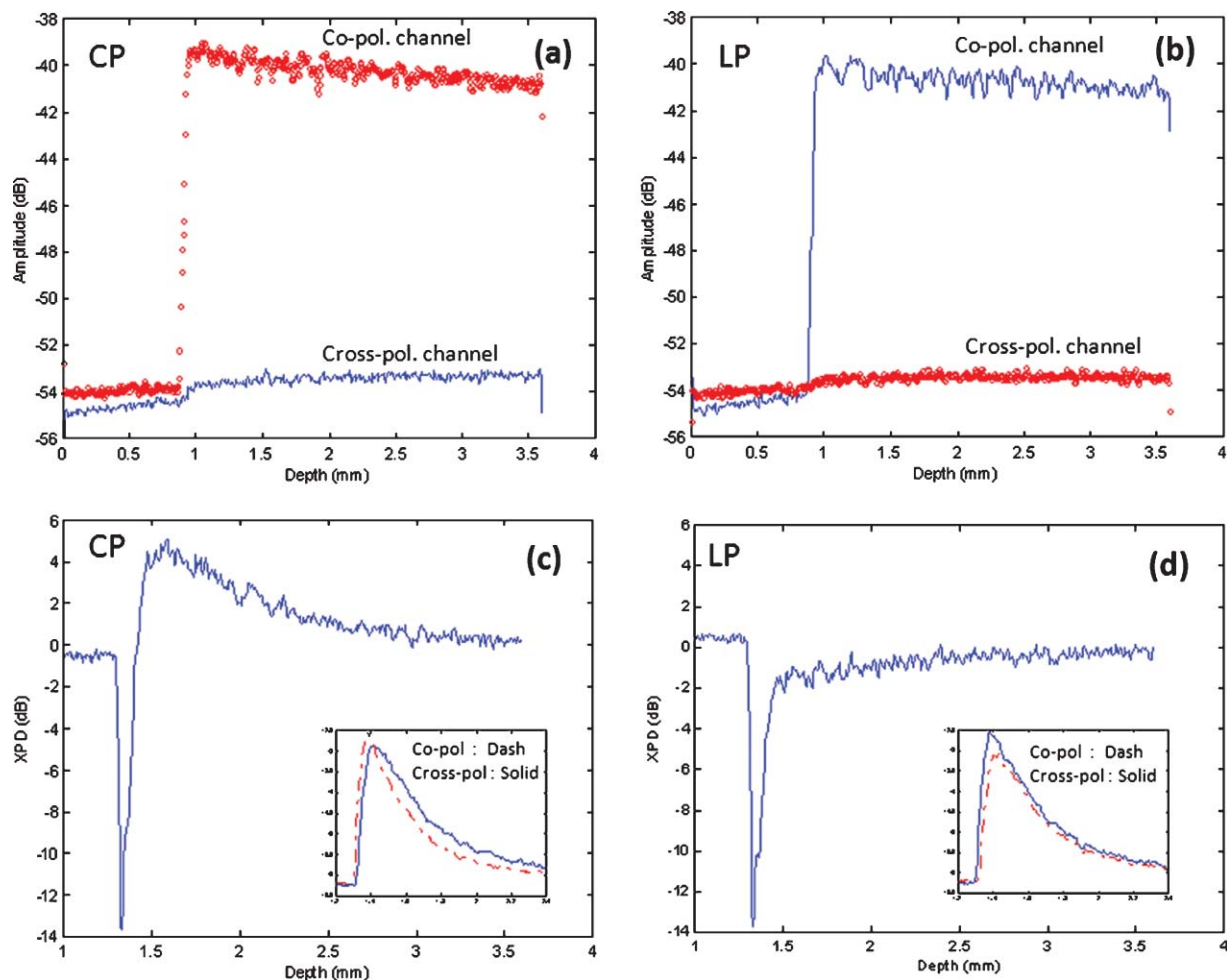
Fig. 2 The backscattering A-lines of small sphere (0.1 μm) from vertical (blue line) and horizontal (red line) polarization channels with (a) CP and (b) LP configurations. XPD lines of large sphere (9.9 μm) with (c) CP and (d) LP configurations where the vertical and horizontal channel A-lines are also shown in the insets with the blue and red color notations. XPD curve in CP configuration goes above the zero line, which indicates polarization memory.
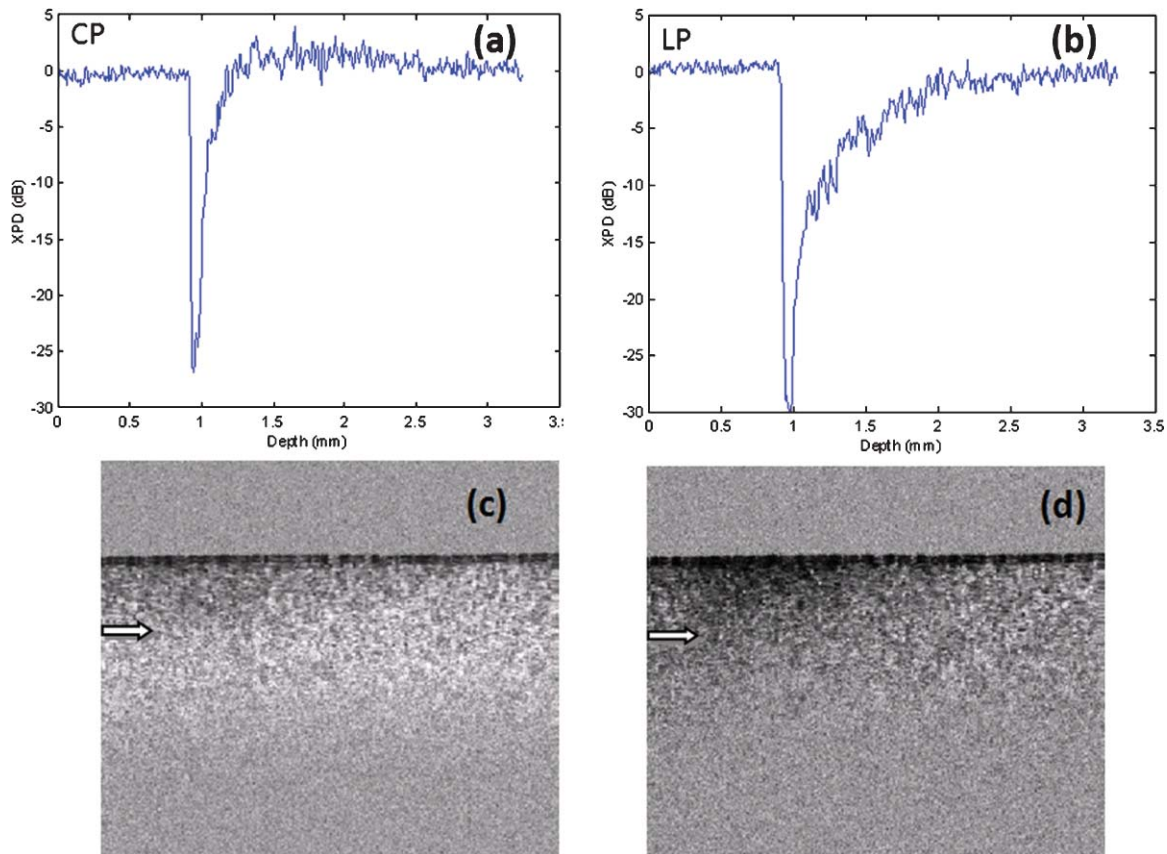
Fig. 3 Dentin tissue images from the sectioned side of a normal human tooth. XPD ratio in Eq. (1) is used as the mapping algorithm. The averaged XPD curves for CP and LP configurations are shown in (a) and (b), respectively. They are similar to the XPD curves of large microsphere phantom. Two-dimensional images of (c) CP and (d) LP have similar textural patterns arising from speckle noise. But, the CP image shows a more whitish band below the surface compared to LP images which indicates XPD > 0 due to PME. Image size is 3.2×2.6 mm (H×W) in air.

alter the scattering properties.[20,24,26,32] We imaged healthy dentin samples. Negative to positive XPD values were mapped with black to white-gray scales to form PS-OCT B-mode image. The depth resolved XPD curves were similar to what we obtained with the large sphere phantom. In Figs. 3(a) and 3(b), we averaged the XPD lines of the dentin along the lateral dimension for CP and LP scans. The averaging was performed after matching the tooth surface pixel of every XPD line to the same depth location according to the segmented tooth-air boundaries. These figures show the same characteristic features as in Figs. 2(c) and 2(d) of the phantom study. The PS-OCT images in CP and LP configurations are shown in Figs. 3(c) and 3(d). The difference in contrast between CP and LP images is indicated by arrows. Beside a high frequency speckle texture modulation, the area below the tooth surface in the CP image appears overall whitish. We used two approaches to verify that this polarization feature originated from PME rather than weak birefringence. In the first approach, we used Stokes vector analysis. Pierce et al.[17] showed that even in the weak birefringence case, Stokes analysis can still produce a linear phase retardation curve with respect to the imaging depth. A slope value was obtained to assess the healthy skin and malignant cancer progression after averaging many axial scans along the lateral dimension. We attempted to apply Stokes vector analysis to the dentin data, but we were not able to observe a linear phase retardation slope. Therefore, the observed image feature should not be interpreted by weak birefringence. In the second approach, we used LP configuration as the "control" experiment. From LP OCT images, the polarization feature of a whitish band structure, as seen in CP images, was not observed. The same tissue regions indicated by the white arrows in Figs. 3(c) and 3(d) appear darker in the LP scan than that in the CP scan. The corresponding XPD curve in Fig. 3(b) remains negative and asymptotically approaches zero XPD line at deeper depth. These are quite unique features are agreeable with the PME theory, as well as the phantom study. When imaging enamel with LP light, however, periodic birefringence bands still exist, despite a reduced contrast compared to CP light. We conclude, based on the above investigations, that the polarization behavior from the dentin and enamel in CP OCT scan are governed by different polarization mechanisms. For dentin, it is from the polarization memory effect, and for enamel, it is from birefringence effect.

There is plenty of evidence that optical scattering of caries lesions is different from normal states and it is polarization sensitive.[24,26,32] We performed a study with a demineralization model to assess PME as a potential marker for dentin lesions. A phosphoric acid process to remove crystallized minerals was applied to the sectioned dentin surfaces. This model effectively creates artificial caries similar to bacterial infection. Figures 4(c) and 4(d) show two CP OCT scans across both the dentin and the adjacent enamel. The regular intensity OCT images are shown at the top. The CP PS-OCT images mapped by XPD lines in
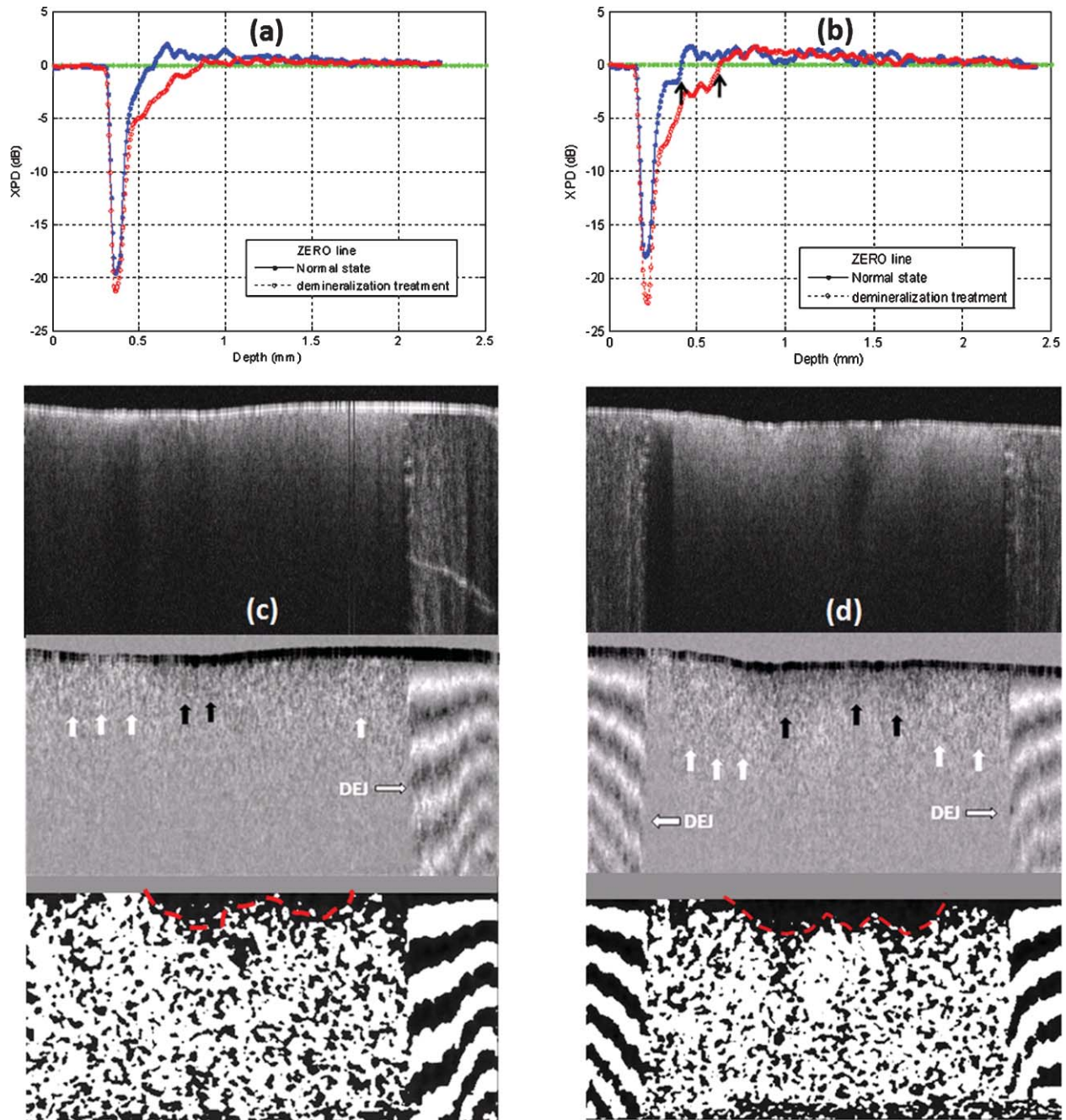
Fig. 4 Two tooth samples imaged after the demineralization process. The image size is about 3.2 × 8 mm in air. (a) and (b) are the averaged XPD curves from treated (red) and intact (blue) area. (c) and (d) show the OCT intensity images (top), the CP PS-OCT images mapped by XPD lines (middle), and the binary images (bottom) with a better visualization of the progression of the acid treatment.

the middle show the different imaging features of dentin and enamel due to the two different polarization behaviors. The alternate bright and dark bands on the right side of Fig. 4(c), and on both sides of Fig. 4(d), are typical features of birefringence in the enamel, while the dim single white band in the middle is a feature from PME in the dentin. DEJ, the junction between dentin and enamel identified as a vertical border, clearly splits the two types of tissues which are much less separable in the intensity mapped OCT images. Birefringence is a well acknowledged effect in PS-OCT. PME is still new and will be examined more in future studies. Both effects could lead to useful medical applications. The middle parts of the CP PS-OCT images near

the surface corresponded to where the phosphoric acid process was applied. These areas appear darker, which imply that some polarization memory is lost. This finding is more clearly seen in the averaged XPD lines in Figs. 4(a) and 4(b), where the red line averages the drug affected region and the blue line averages the normal region. For preprocessing, the XPD line was realigned along the dentin-air surface with an edge detection algorithm prior to averaging. It is interesting to see that after a certain depth, the red XPD line seems to regain its polarization memory. The two arrows shown in Fig. 4(b) point out the depth range where the channel energy reversal occurs at the normal and treated dentin areas. The distance between the two

arrows roughly indicates the progression of the acid treatment. Similar to the analysis of weak birefringence,[17,18] PME can be better estimated through averaging and other filtering processing with a penalty in spatial resolution. Furthermore, PME quantified by XPD ratio has a characteristic zero line, which can serve as a sensitive benchmark for spatial demarcation of dematerialized and normal dentin tissue. The bottom images of Figs. 4(c) and 4(d) are the processed binary images using zero XPD level as the threshold to enhance the contrast. It can be seen that the energy in the cross-polarization channel exceeds that in the co-polarization channel in most parts of the dentin images except the dark areas near the middle of the dentin surface. Estimated spatial boundaries of acid progression are drawn in red dashed lines. A 5×5 medium filter and a 3×3 linear statistical de-speckle filter were used before the binary image process to reduce speckle noise.

5 Summary

In summary, we have reported to our knowledge the first observation of polarization memory effect in scattering phantoms and dentin tissues using PS-OCT. Experimental designs and analytical methods are given in order to differentiate the PME and weak birefringence which are of different origins. From the application aspect, polarization-sensitive detection could be useful for the investigation of the ultrastructural features in the demineralization and remineralization processes and for the diagnosis of dental caries.

As a follow-up in future research work, it would be interesting to extend the study to the remineralization study to evaluate the efficacy of rehabilitation drugs. As a blind test, two tooth pastes, one with plain (expected to do nothing) and the second containing amorphous calcium phosphate, for example, that expected to put mineral back into the etched dentin can be used. PS-OCT using PME analysis may prove to be a useful *in vitro* method to evaluate the efficacy of drugs for repairing dental caries in addition to the potential application for the early caries detection. This remineralization and demineralization testing may be applied on extracted teeth repeatedly without the need to destroy them for investigation, such as in the case of regular optical or scanning electron microscopic imaging.

From the technology prospective, this study was performed with a less sensitive time-domain OCT. It would be helpful to use a volumetric imaging protocol with more sensitive Fourier-domain OCT technology to study the changes before and after mineralization treatment. This way, the tissue locations can be registered for a more accurate comparison.

References

1. D. Huang, E. A. Swanson, C. P. Lin, J. S. Schuman, W. G. Stinson, W. Chang, M. R. Hee, T. Flotte, K. Gregory, C. A. Puliafito, and J. G. Fujimoto, "Optical coherence tomography," *Science* **254**(5035), 1178–1181 (1991).
2. J. F. de Boer, T. E. Milner, M. J. C. vanGemert, and J. S. Nelson, "Two-dimensional birefringence imaging in biological tissue by polarization-sensitive optical coherence tomography," *Opt. Lett.* **22**(12), 934–936 (1997).
3. J. F. De Boer, T. E. Milner, and J. S. Nelson, "Determination of the depth-resolved Stokes parameters of light backscattered from turbid media by use of polarization-sensitive optical coherence tomography," *Opt. Lett.* **24**(5), 300–302 (1999).
4. C. K. Hitzenberger, E. Gotzinger, M. Sticker, M. Pircher, and A. F. Fercher, "Measurement and imaging of birefringence and optic axis orientation by phase resolved polarization sensitive optical coherence tomography," *Opt. Express* **9**(13), 780–790 (2001).
5. G. Yao and L. V. Wang, "Two-dimensional depth-resolved Mueller matrix characterization of biological tissue by optical coherence tomography," *Opt. Lett.* **24**(8), 537–539 (1999).
6. S. L. Jiao, G. Yao, and L. H. V. Wang, "Depth-resolved two-dimensional Stokes vectors of backscattered light and Mueller matrices of biological tissue measured with optical coherence tomography," *Appl. Opt.* **39**(34), 6318–6324 (2000).
7. Y. Yasuno, S. Makita, Y. Sutoh, M. Itoh, and T. Yatagai, "Birefringence imaging of human skin by polarization-sensitive spectral interferometric optical coherence tomography," *Opt. Lett.* **27**(20), 1803–1805 (2002).
8. J. F. de Boer, S. M. Srinivas, A. Malekafzali, Z. P. Chen, and J. S. Nelson, "Imaging thermally damaged tissue by polarization sensitive optical coherence tomography," *Opt. Express* **3**(6), 212–218 (1998).
9. B. H. Park, C. Saxer, S. M. Srinivas, J. S. Nelson, and J. F. de Boer, "*In vivo* burn depth determination by high-speed fiber-based polarization sensitive optical coherence tomography," *J. Biomed. Opt.* **6**(4), 474–479 (2001).
10. C. E. Saxer, J. F. de Boer, B. H. Park, Y. H. Zhao, Z. P. Chen, and J. S. Nelson, "High-speed fiber-based polarization-sensitive optical coherence tomography of *in vivo* human skin," *Opt. Lett.* **25**(18), 1355–1357 (2000).
11. S. L. Jiao and L. H. V. Wang, "Jones-matrix imaging of biological tissues with quadruple-channel optical coherence tomography," *J. Biomed. Opt.* **7**(3), 350–358 (2002).
12. B. Cense, H. C. Chen, B. H. Park, M. C. Pierce, and J. F. de Boer, "*In vivo* birefringence and thickness measurements of the human retinal nerve fiber layer using polarization-sensitive optical coherence tomography," *J. Biomed. Opt.* **9**(1), 121–125 (2004).
13. S. G. Guo, J. Zhang, L. Wang, J. S. Nelson, and Z. P. Chen, "Depth-resolved birefringence and differential optical axis orientation measurements with fiber-based polarization-sensitive optical coherence tomography," *Opt. Lett.* **29**(17), 2025–2027 (2004).
14. E. Gotzinger, M. Pircher, and C. K. Hitzenberger, "High speed spectral domain polarization sensitive optical coherence tomography of the human retina," *Opt. Express* **13**(25), 10217–10229 (2005).
15. M. Yamanari, S. Makita, V. D. Madjarova, T. Yatagai, and Y. Yasuno, "Fiber-based polarization-sensitive Fourier domain optical coherence tomography using B-scan-oriented polarization modulation method," *Opt. Express* **14**(14), 6502–6515 (2006).
16. M. Yamanari, Y. Lim, S. Makita, and Y. Yasuno, "Visualization of phase retardation of deep posterior eye by polarization-sensitive swept-source optical coherence tomography with 1-microm probe," *Opt. Express* **17**(15), 12385–12396 (2009).
17. M. C. Pierce, J. Strasswimmer, B. H. Park, B. Cense, and J. F. de Boer, "Birefringence measurements in human skin using polarization-sensitive optical coherence tomography," *J. Biomed. Opt.* **9**(2), 287–291 (2004).
18. J. Strasswimmer, M. C. Pierce, B. H. Park, V. Neel, and J. F. de Boer, "Polarization-sensitive optical coherence tomography of invasive basal cell carcinoma," *J. Biomed. Opt.* **9**(2), 292–298 (2004).
19. E. Gotzinger, M. Pircher, W. Geitzenauer, C. Ahlers, B. Baumann, S. Michels, U. Schmidt-Erfurth, and C. K. Hitzenberger, "Retinal pigment epithelium segmentation by polarization sensitive optical coherence tomography," *Opt. Express* **16**(21), 16410–16422 (2008).
20. B. W. Colston, Jr., U. S. Sathyam, L. B. DaSilva, M. J. Everett, P. Stroeve, and L. L. Otis, "Dental OCT," *Opt. Express* **3**(6), 230–238 (1998).
21. B. W. Colston, Jr., M. J. Everett, L. B. Da Silva, L. L. Otis, P. Stroeve, and H. Nathal, "Imaging of hard- and soft-tissue structure in the oral cavity by optical coherence tomography," *Appl. Opt.* **37**(16), 3582–3585 (1998).

22. X. J. Wang, T. E. Milner, J. F. de Boer, Y. Zhang, D. H. Pashley, and J. S. Nelson, "Characterization of dentin and enamel by use of optical coherence tomography," *Appl. Opt.* **38**(10), 2092–2096 (1999).
23. A. Baumgartner, S. Dichtl, C. K. Hitzenberger, H. Sattmann, B. Robl, A. Moritz, A. F. Fercher, and W. Sperr, "Polarization-sensitive optical coherence tomography of dental structures," *Caries Res.* **34**(1), 59–69 (2000).
24. D. Fried, J. Xie, S. Shafi, J. D. B. Featherstone, T. M. Breunig, and L. Charles, "Imaging caries lesions and lesion progression with polarization sensitive optical coherence tomography," *J. Biomed. Opt.* **7**(4), 618–627 (2002).
25. Y. Chen, L. Otis, D. Piao, and Q. Zhu, "Characterization of dentin, enamel, and carious lesions by a polarization-sensitive optical coherence tomography system," *Appl. Opt.* **44**(11), 2041–2048 (2005).
26. S. K. Manesh, C. L. Darling, and D. Fried, "Polarization-sensitive optical coherence tomography for the nondestructive assessment of the remineralization of dentin," *J. Biomed. Opt.* **14**(4), 044002 (2009).
27. F. C. MacKintosh, J. X. Zhu, D. J. Pine, and D. A. Weitz, "Polarization memory of multiply scattered light," *Phys. Rev.* **40**(13), 9342–9345 (1989).
28. X. Ni and R. R. Alfano, "Time-resolved backscattering of circularly and linearly polarized light in a turbid medium," *Opt. Lett.* **29**(23), 2773–2775 (2004).
29. J. Perdigao and E. J. Swift, "Analysis of dental adhesive systems using scanning electron microscopy," *Int. Dent. J.* **44**(4), 349–359 (1994).
30. Y. Chen, L. Otis, and Q. Zhu, "Polarization memory effect in the polarization-sensitive optical coherence tomography system," *Proc. SPIE* **6429**, 64290K (2007).
31. X. Ni, S. A. Kartazayeva, W. Wang, W. Cai, S. K. Gayen, and R. R. Alfano, "Polarization memory effect and visibility improvement of targets in turbid media," *Proc. SPIE* **6434**, 64340N (2007).
32. C. Mujat, M. H. van der Veen, J. L. Ruben, J. J. ten Bosch, and A. Dogariu, "Optical path-length spectroscopy of incipient caries lesions in relation to quantitative light-induced fluorescence and lesion characteristics," *Appl. Opt.* **42**(16), 2979–2986 (2003).